ACS APPLIED ENERGY MATERIALS

www.acsaem.org Article

Formation of a Stable Solid-Electrolyte Interphase at Metallic Lithium Anodes Induced by $LiNbO_3$ Protective Layers

Ming Jiang, Qian Zhang, Dmitri L. Danilov, Rüdiger-A. Eichel, and Peter H. L. Notten*

Cite This: ACS Appl. Energy Mater. 2021, 4, 10333−10343 Read Online

ACCESS | Metrics & More | Article Recommendations | Supporting Information

ABSTRACT: The stability of solid-electrolyte interphase (SEI) surface films at Li-metal anodes is crucial for the safe and durable operation of lithium-metal batteries (LMBs). By combining Li-metal anodes with high-performance Ni-rich transition-metal oxide cathodes, LMBs can meet the goal of a high specific energy density of more than 500 Wh kg^{-1}. However, Li-metal anodes suffer from serious problems, especially the nonuniform lithium deposition and uncontrollable SEI formation. In this work, Li-metal anodes were protected by thin-film $LiNbO_3$ coatings. Full cells composed of protected Li-metal anodes and Li-$Ni_{0.6}Co_{0.2}Mn_{0.2}O_2$ cathodes were examined electrochemically and by physical characterization methods. Postmortem analyses of pristine and prolonged cycled Li-metal anodes were performed. The results revealed the formation of more stable SEI films at the protected Li-metal anodes in comparison to unprotected electrodes. Consequently, the $LiNbO_3$ layers improved the cycle-life performance of Li-metal anodes in LMBs. Furthermore, X-ray photoelectron spectroscopy (XPS) analyses showed that the reduction of metallic ions stemming from the Ni-rich cathodes was also inhibited by the protective $LiNbO_3$ layers, thereby further controlling the degradation of Li-metal anodes.

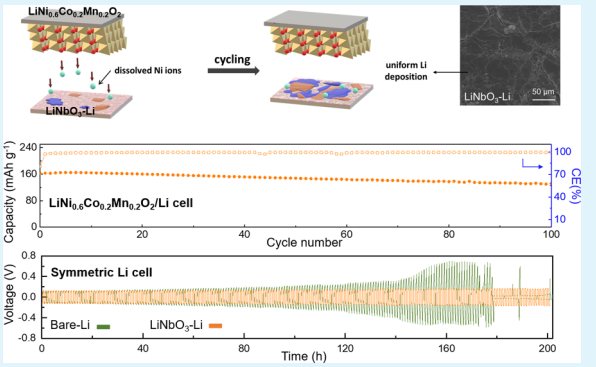

KEYWORDS: *lithium-metal anode, lithium niobate, solid-electrolyte interphase, Ni-rich cathode, crossover, lithium-ion battery*

INTRODUCTION

Lithium-ion batteries (LIBs) are commercially successful and intensively studied over several decades, thanks to the growing number of energy storage applications, including portable devices and (hybrid) electric vehicles.[1−3] Nevertheless, the development of conventional LIBs, which are based on the intercalation chemistry of both electrodes, is gradually approaching the capacity limit of about 300 Wh kg^{-1}.[4] The demand for rechargeable batteries with a higher energy density is therefore of crucial importance for future applications.

Considering Li metal offers a very high theoretical specific capacity as an anode of 3860 mAh g^{-1} at the lowest redox potential of 0 V vs Li^+/Li, lithium-metal secondary batteries are likely to be the most promising alternative for the next generation of LIBs.[5,6] In this regard, Li-metal electrodes are considered the ultimate goal as anode materials in rechargeable batteries. In combination with high-performance Ni-rich nickel−cobalt−manganese (NCM)-layered oxides, such a new battery system is expected to deliver a capacity of more than 500 Wh kg^{-1}.[77] Despite these advantages, the remaining challenges associated with serious safety concerns severely constrain further commercialization of Li-metal anodes in LIBs.[8−10]

On the one hand, Li, by nature, has an extremely high reactivity toward organic electrolytes. Multiple side reactions spontaneously occur at metallic lithium electrodes in contact with the electrolyte, leading to numerous byproducts at the anode surface. These side reactions will be accelerated during battery operations, resulting in an even increased electrolyte consumption and, consequently, severe battery degradation.[11] Furthermore, uneven Li-metal deposition will lead to unfavorable dendrite formation, generating severe safety issues, such as internal short circuiting and thermal runaway.[12] Therefore, unlike graphite anodes that form a relatively stable solid-electrolyte interphase (SEI), the SEI formation at Li-metal anodes is rather uncontrolled and accompanied by the growth of a surface with a highly porous morphology.[13]

Many approaches have been adopted to tailor the surface of Li-metal anodes by controlling both the SEI formation and Li-metal deposition morphology.[14−17] Most studies only focused on symmetric metallic Li cells or Li/Cu cells where Cu is used as a current collector.[18−20] However, the influence of cathode materials on the electrochemistry of Li-metal anodes is rarely

Received: July 31, 2021
Accepted: August 24, 2021
Published: September 2, 2021

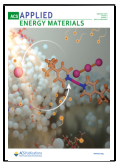

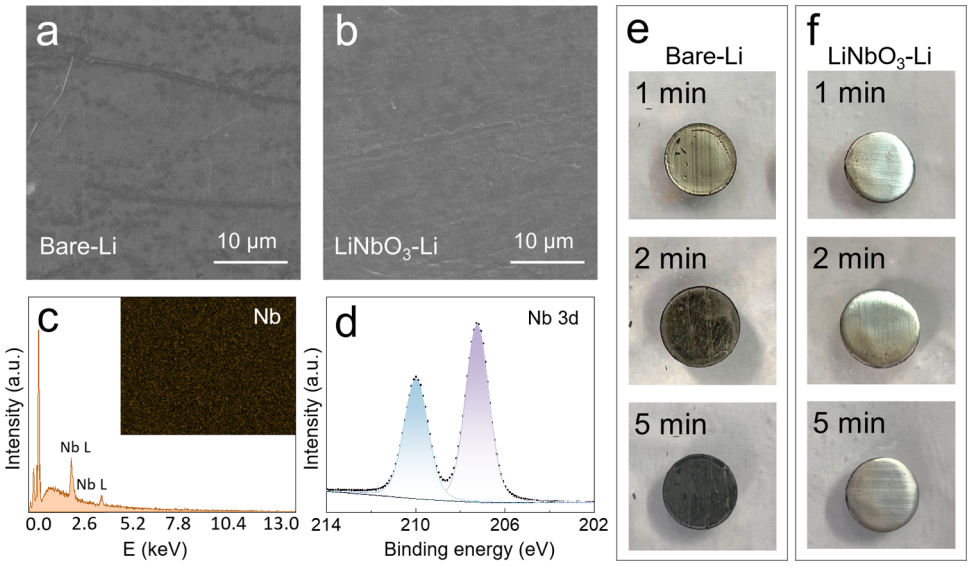

Figure 1. SEM images of (a) pristine bare Li metal and (b) pristine $LiNbO_3$-coated Li-metal electrode. (c) EDX spectrum and elemental Nb mapping of the $LiNbO_3$ protective layer. (d) XPS spectra of the as-deposited amorphous $LiNbO_3$ layer and optical images of the Li corrosion process under ambient atmospheric conditions of (e) bare Li metal and (f) $LiNbO_3$-coated Li metal.

discussed. Notably, it has been identified that the surface reactions at the anode show a strong correlation with the cathode material.[21,22] It was found that applying various cathode materials leads to different SEI surface layers at the anodes. Up to now, several reports have presented this so-called crossover effect between the cathode and anode in LIB chemistries, such as $LiCoO_2$/Li,[23] $LiFePO_4$/Li,[24] and $LiNi_{0.5}Co_{0.3}Mn_{0.2}O_2$/graphite[21] cells, while a detailed analysis of Ni-rich NCM/Li batteries is still lacking.

A single report discussed the influence of three different cathode materials ($LiNi_{0.5}Mn_{1.5}O_4$, $LiNi_{0.6}Co_{0.2}Mn_{0.2}O_2$, and $LiFePO_4$) on the morphology of Li-metal deposition, but the investigation of the SEI formation was somewhat limited.[25] Another report has recently presented results of cathode−anode crossover, occurring in $LiNi_{0.9}Co_{0.05}Mn_{0.05}O_2$/Li and $LiNi_{0.9}Co_{0.05}Mn_{0.05}O_2$/graphite cells.[26] However, this work only explored the SEI formation for the cells (dis)charged up to 50 cycles, which is unrepresentative for long-life batteries as some effects induced by the cathode, such as the dissolution of transition-metal ions, can only be appropriately detected during prolonged cycling. In view of the growing number of strategies to improve Li-metal anode operation, it is therefore of vital importance to understand the SEI evolution at metallic Li anodes.

In this paper, $LiNbO_3$, a solid-state electrolyte possessing a high ionic conductivity, is proposed as the protective layer for Li-metal anodes. After protection, the Li-metal anodes show an enhanced stripping/plating stability in symmetric cells, indicating that the surface reactions are well controlled by the presence of these $LiNbO_3$ layers. Subsequently, $LiNi_{0.6}Co_{0.2}Mn_{0.2}O_2$/Li cells were assembled and investigated. The electrochemical performances of cells using bare Li anodes and $LiNbO_3$-coated Li anodes are compared comprehensively. Particular attention is drawn to the differences of the SEI surface film evolution and Li-metal deposition morphology on both types of anodes during initial and prolonged cycling. The distinct responses of Li anodes toward the crossover induced by the cathode have been investigated, and the insights regarding the optimization role of $LiNbO_3$ protective layers in achieving the suppressed SEI formation are revealed.

EXPERIMENTAL SECTION

$LiNbO_3$-Coated Li-Metal Electrodes. A Li-metal foil with 0.75 mm thickness was purchased from Alfa Aesar, commercial Ni-rich $LiNi_{0.6}Co_{0.2}Mn_{0.2}O_2$ powder (NCM) was obtained from Tianjin B&M Science and Technology (China), and $LiNbO_3$ sputtering targets were obtained from Lesker (U.K.). The whole process was operated in a glovebox, avoiding any exposure to air. $LiNbO_3$ thin films were deposited on the Li foil by radio frequency (RF) magnetron sputtering. The distance between the substrate and target was fixed at 15 cm. The substrates kept rotating at a speed of 20 rpm to guarantee homogeneous deposition. The sputtering process was performed in an Ar atmosphere under a chamber pressure of 5 mTorr and 60 W sputtering power. The thickness of the obtained $LiNbO_3$ layers was determined to be 30 nm at a deposition rate of ∼2 Å min^{-1}.

Material Characterization. Scanning electron microscopy (SEM) and energy-dispersive X-ray spectroscopy (EDX) experiments were carried out using a Quanta FEG 650 (FEI) environmental scanning electron microscope operated at a voltage of 20 kV. X-ray diffraction (XRD) measurements were carried out between 10 and 80° using Cu Kα radiation using an EMPYREAN X-ray diffractometer (Panalytical, The Netherlands). X-ray photoelectron spectroscopy (XPS) was performed by a Thermo Scientific K-Alpha instrument with a monochromatic X-ray source (Al Kα). The anodes were dismantled from the cycled cells, rinsed several times by dimethyl carbonate (DMC) solvent and ethanol absolute, and dried in the glovebox overnight before XPS measurements.

Electrochemical Measurements. The electrochemical performance was investigated in Swagelok cells. All electrochemical tests were performed in an MKF120 climate chamber (Binder, Germany), using a VMP3 potentiostat (Bio-Logic, France). For the symmetric Li cells, Li-metal foils with a diameter of 12 mm were used as both working and counter/reference electrodes. The symmetric cells were subjected to pulse (dis)charging at current densities of 0.5 and 1 mA cm^{-2} during 0.5 h for each step.

For the complete cells, NCM cathode slurries were prepared by mixing the commercial NCM powder with carbon black (Super P, Alfa Aesar) and a poly(vinylidene fluoride) binder (PVDF, Sigma-Aldrich) at a weight ratio of 8:1:1. The mixture was then dissolved in *N*-methyl pyrrolidone (NMP). The slurry was uniformly coated onto aluminum foils and dried overnight at 90 °C and then cut into discs of

https://doi.org/10.1021/acsaem.1c02278
ACS Appl. Energy Mater. 2021, 4, 10333−10343

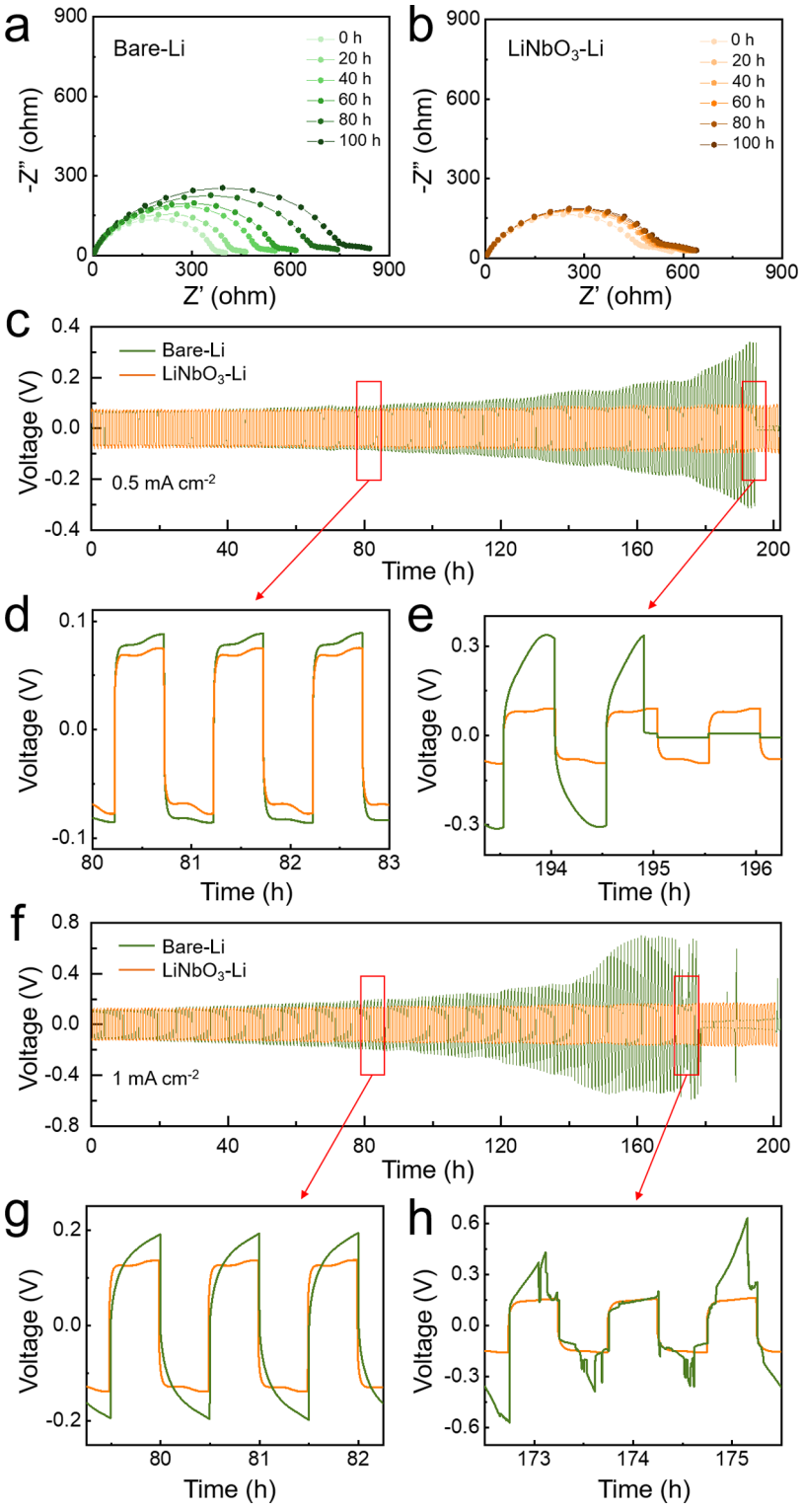

Figure 2. EIS spectra of symmetric Li cells with (a) bare Li and (b) $LiNbO_3$-protected Li during storage at room temperature. (c) Overview of galvanostatic cycling experiments of symmetric Li cells at 0.5 mA cm^{-2} and at a higher magnification after (d) 80 h cycling and after (e) 195 h cycling. (f) Overview of galvanostatic profiles of symmetric Li cells cycled at 1 mA cm^{-2} and in more detail after (g) 80 h cycling and after (h) 175 h cycling.

12 mm diameter. Bare metallic Li and $LiNbO_3$-coated Li-metal electrodes were used as anodes in full cells. $LiPF_6$ (1 M) in a 1:1 mixed solvent of ethylene carbonate (EC)/dimethyl carbonate (DMC) (BASF) was used as an electrolyte. Galvanostatic cycling was performed in the voltage range of 3.0−4.3 V vs Li^+/Li. Electrochemical impedance spectroscopy (EIS) tests were conducted with an amplitude of 10 mV in the frequency range of 200 kHz to 0.1 Hz.

RESULTS AND DISCUSSION

Figure 1a,b shows the SEM results of the surface morphology of bare Li metal and $LiNbO_3$-protected Li metal. The surface

https://doi.org/10.1021/acsaem.1c02278
ACS Appl. Energy Mater. 2021, 4, 10333−10343

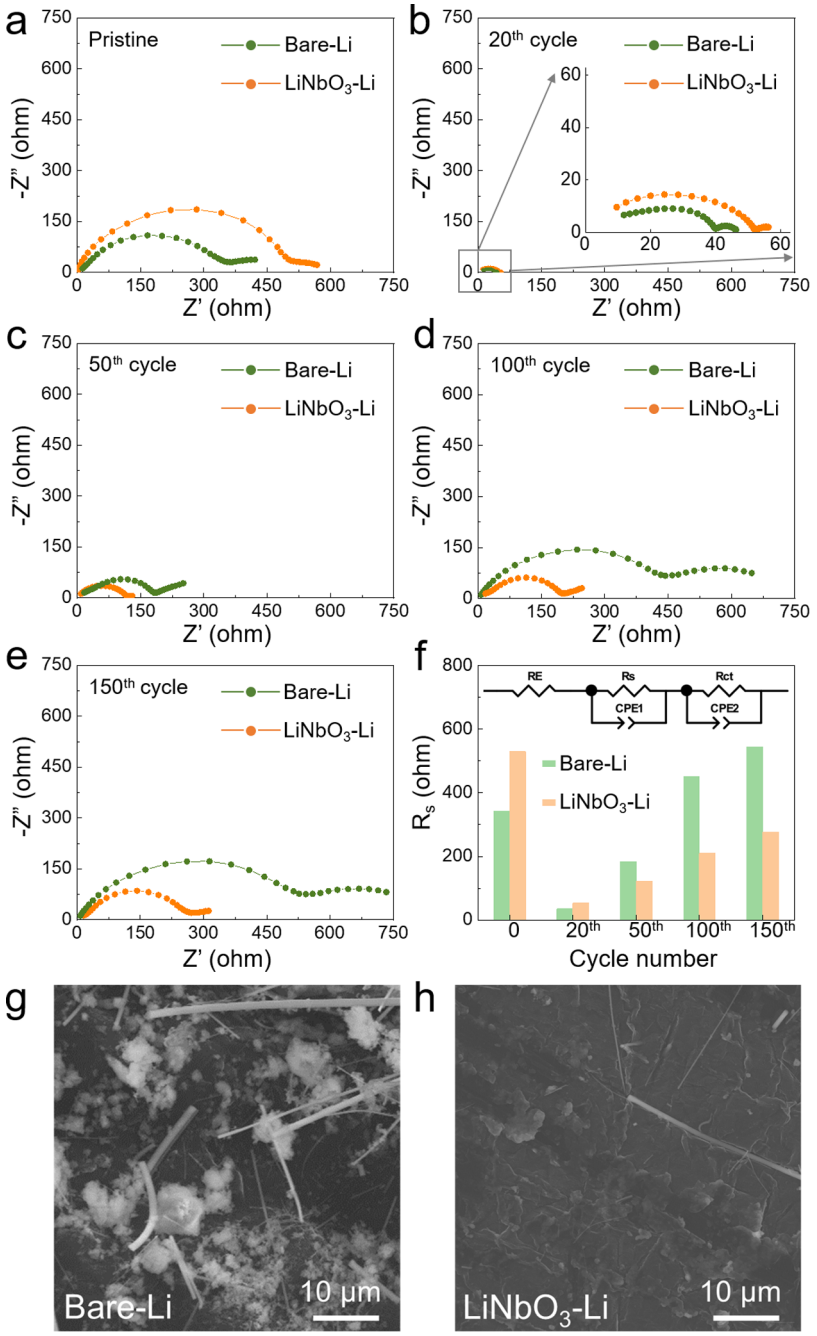

Figure 3. EIS spectra of symmetric Li cells at (a) pristine state, (b) 20th cycle, (c) 50th cycle, (d) 100th cycle, and (e) 150th cycle. (f) Equivalent circuit and R_s evolution during cycling. SEM images of cycled (g) bare Li and (h) $LiNbO_3$-protected Li.

of bare Li demonstrates an overall smooth surface morphology with several intrinsic microscratches. After deposition of $LiNbO_3$, it can be seen that the layer has been homogeneously and conformally coated onto the Li metal. This layer compactly covers the microscratches at the Li-metal surface. It should be noted that the $LiNbO_3$ layer prepared via sputtering at room temperature is amorphous. No diffraction peaks can be identified in the XRD pattern (Figure S1). The EDX spectrum of the obtained $LiNbO_3$-Li sample shows a strong Nb signal. The mapping analysis reveals a uniform elemental distribution of the $LiNbO_3$ layer (Figure 1c).

The elemental valence state of Nb in the amorphous $LiNbO_3$ layer was also analyzed by XPS. The Nb 3d spectra shown in Figure 1d imply that Nb ions exist in the amorphous $LiNbO_3$ layer on Li metal as Nb^{5+}; the peaks located at 207.2 and 210.5 eV are attributed to Nb^{5+} $3d_{5/2}$ and Nb^{5+} $3d_{3/2}$, respectively. In addition, to evaluate the compactness of the coating, both protected and unprotected metal samples were placed under ambient atmospheric conditions at 25 °C for 5 min. It is well known that Li metal is highly reactive with oxygen, nitrogen, and water in the air. Thus, after exposure, the surface of the bare Li sample rapidly gets tarnished within a few minutes to become ultimately black after 5 min (Figure 1e). The color change is associated with multiple compounds formed at the Li-metal surface, including Li_2CO_3, Li_2O, LiOH, Li_3N, etc.[9]

In contrast, the surface of $LiNbO_3$-protected Li metal remained stable. It nearly maintained its original metallic

https://doi.org/10.1021/acsaem.1c02278
ACS Appl. Energy Mater. 2021, 4, 10333−10343

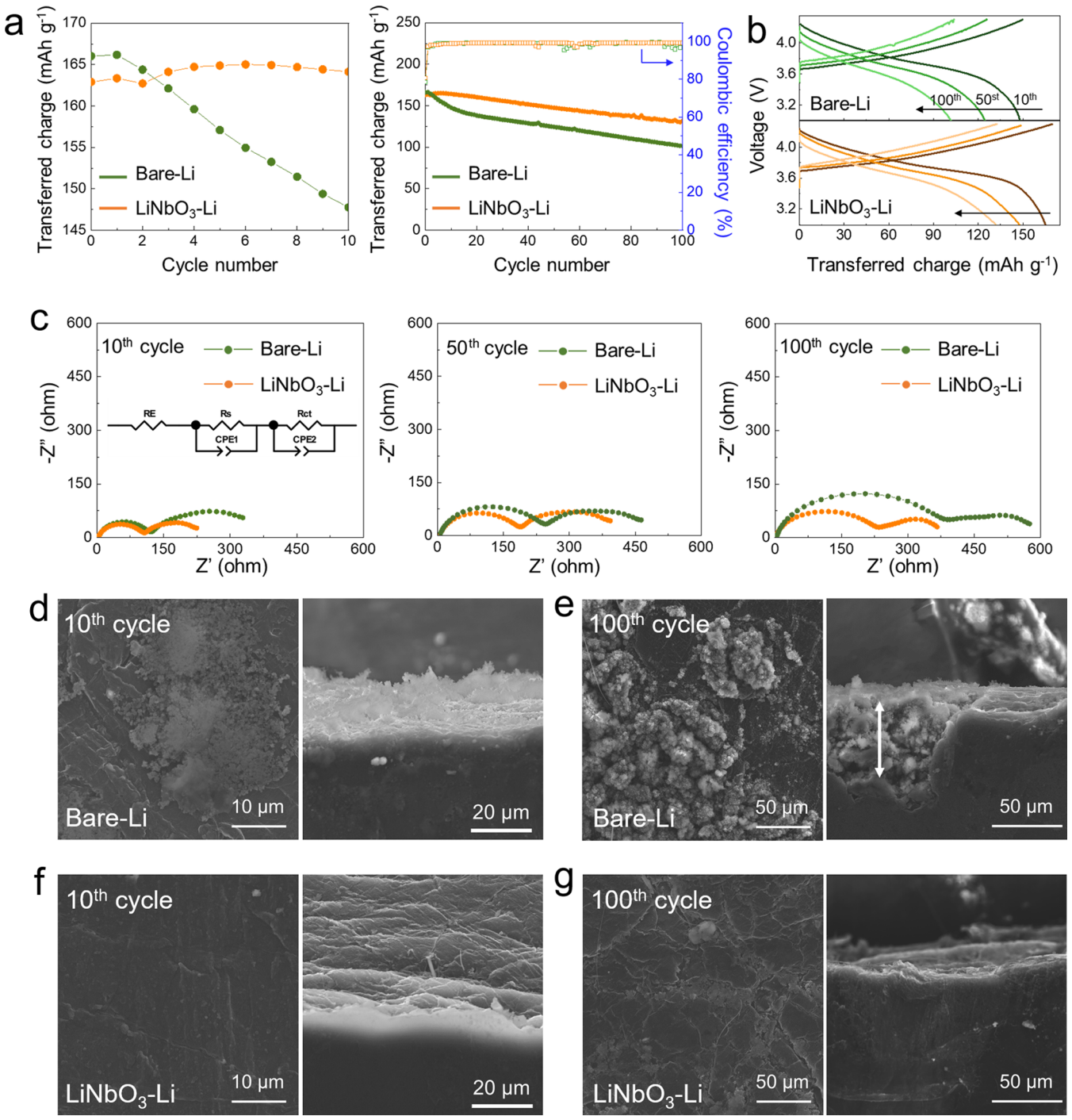

Figure 4. (a) Galvanostatic (1C) cycling of the initial 10 and 100 cycles and (b) voltage profiles of NCM/Li cells at various cycles. (c) EIS spectra of the Li anodes after cycling. Top view and cross-sectional view of SEM images of the bare Li anode after (d) 10 cycles and (e) 100 cycles. Top view and cross-sectional view of SEM images of the $LiNbO_3$-Li anode after (f) 10 cycles and (g) 100 cycles.

shining state after 5 min of exposure to air (Figure 1f). This observation indicates that a homogeneous coating of $LiNbO_3$ might be effective as a protective layer at metallic Li electrodes.

Lithium stripping and plating were performed in symmetric Li−Li cells to investigate the interfacial stability of Li-metal electrodes. Figure 2 shows the evolution of the cell impedance with storage time, keeping the cells under open-circuit conditions. The impedance of the bare Li cell (Figure 2a) increases significantly over time. This phenomenon is caused by the spontaneous reaction of metallic Li with the electrolyte, leading to the continuous growth of the passive layer. However, the impedance of the symmetric $LiNbO_3$-Li cell (Figure 2b) shows that the charge-transfer resistance reached a highly stable state after ~20 h storage. This can be attributed to the effective isolation properties of the $LiNbO_3$ coating, which suppresses parasitic reactions at the Li-metal surface. Notably, the pristine $LiNbO_3$-Li symmetric cell (Figure 2b) shows a larger initial resistance, owing to the additional ionic conductivity of the protective coating. It has been extensively reported that Li metal is thermodynamically unstable in

https://doi.org/10.1021/acsaem.1c02278
ACS Appl. Energy Mater. 2021, 4, 10333−10343

organic solvents.[13] Thus, protecting Li-metal electrodes from side reactions with the electrolyte is essential to stabilize the anodes of LMBs.

The stability of the Li stripping/plating process was further investigated in symmetric cells. Figure 2c shows the voltage profiles of bare Li (green) and $LiNbO_3$-Li (orange) symmetric cells cycled in a commercial electrolyte (1 M $LiPF_6$ in 1:1 EC/DMC) at a current density of 0.5 mA cm^{-1} during 0.5 h for each step. It can be seen that the bare Li symmetric cell revealed significantly enlarged overpotentials with increasing cycling time. As shown in Figure 2d, the stripping/plating overpotentials after about 80 h are very similar for both symmetric cells (160 mV vs Li^+/Li). However, the overpotential of the bare Li cell continuously increases up to 600 mV at the end of cycling and encounters a sudden voltage drop after 195 h (green curve in Figure 2e), implying a detrimental cell failure caused by short circuits. The unstable voltage is attributed to the nonuniform Li-metal nucleation and SEI formation during cycling. The end of life is clearly related to the formation of detrimental short circuits. In contrast, the performance of the $LiNbO_3$-Li symmetric cell (orange curve) demonstrates improved stability with no sign of any short circuits even after 200 h of cycling.

Remarkably, at a higher current density of 1 mA cm^{-2}, the $LiNbO_3$-Li symmetric cell still demonstrates highly stable behavior with negligible overpotential changes. The overview of Figure 2f shows a sharp contrast between the two voltage profiles. The summation of the overpotentials, occurring during charging and discharging the bare Li symmetric cell, increases from 400 mV after 80 h (Figure 2g) to around 900 mV after 175 h (Figure 2h). Also, the significant increase of overpotential was followed by considerable noisy fluctuations at 173 h (Figure 2h). Cell failure can be observed after 180 h, whereas for the $LiNbO_3$-protected Li cell, the voltage profile at a higher current density shows similar behavior to that of 0.5 mA cm^{-2}. In this case, the overpotentials only slightly increase from 220 to 250 mV at the end of cycling. The much longer cycle life and improved stability of the $LiNbO_3$-Li symmetric cells show that the $LiNbO_3$ protective layer facilitates unobstructed Li-ion transport, leading to homogeneous Li deposits and only moderate volume expansion during the stripping and plating process.

EIS measurements have been conducted with both symmetric cells after various cycles (Figure 3a–e). The adopted equivalent circuit and the surface film resistance obtained by spectra fitting are shown in Figure 3f. The bare Li and $LiNbO_3$-coated Li have shown surface film resistance of 341 and 529 Ω for the pristine cells, respectively (Figure 3a). The larger resistance of pristine $LiNbO_3$-Li must be attributed to the deposited $LiNbO_3$ layer, which acts as a barrier for Li^+-ion transport, in contrast to the bare Li case. Figure 3b shows that after the initial cycles of stripping and plating, both symmetric cells experience a significant reduction of R_s to 35 and 53 Ω. Subsequently, the R_s of the $LiNbO_3$-Li cell increases from 122 Ω after 50 cycles to 276 Ω after 150 cycles, while for the bare Li symmetric cell, a much larger increase of R_s is observed. The impedance of the bare Li cell gradually rises from 183 (50th cycle) to 543 Ω (150th cycle), displaying ∼2 times higher resistance than that of the $LiNbO_3$-Li cell after long-term cycling.

The electrode morphologies have been further examined by SEM after 200 h of stripping and plating. The intensively cycled bare Li cell reveals a notably rough and porous surface morphology (Figure 3g) with Li dendrites and a needle-like structured Li surface layer. The Li structures on the bare Li surface have been considered as "death Li", losing electronic contact with the bulk Li foil, and are associated with the sharp impedance increase during cycling. Contrastingly, the surface of the cycled $LiNbO_3$-protected Li cell maintains a relatively flat and compact structure (Figure 3h). It is also found that the surface of the $LiNbO_3$-Li electrode adopts a slightly convex shape after cycling compared to its pristine state. This observation suggests the presence of internal stress induced by the Li volume expansion underneath the $LiNbO_3$ layer. These results, therefore, demonstrate that the $LiNbO_3$ coating with intrinsic high ionic conductivity effectively provides smooth Li transportation through the $LiNbO_3$/Li interface. This leads to a homogeneous Li stripping/plating process with relatively uniform Li deposition.

The electrochemical performance and corresponding material characterization of full cells with commercial Ni-rich NCM cathodes and Li-metal anodes have been investigated for the potential practicability of $LiNbO_3$-protected Li anodes. Figure 4a demonstrates the cycling performance of the two NCM/Li cells cycled at 1C rate within the voltage range of 3.0–4.3 V vs Li^+/Li. The cycling profiles of the first 10 cycles highlight the rapid degradation of the NCM/Li cell with the bare Li anode (green symbols). Initially, the cells with the bare Li and the $LiNbO_3$-Li anode deliver similar specific capacities of 166 and 164 mAh g^{-1}, respectively. After 100 cycles, the bare Li cell shows a higher degradation rate with 60% capacity retention, leading to a capacity of 101.3 mAh g^{-1}. In contrast, an improved cycling performance is achieved in the cell with the $LiNbO_3$-protected Li anode. The cell exhibits a discharge capacity of 131.6 mAh g^{-1} after 100 cycles (capacity retention of 80%).

The voltage profiles of both cells at the 10th, 50th, and 100th cycles are shown in Figure 4b, revealing smaller transferred charge upon cycling and a higher voltage decay of the cell with the bare Li anode than that of the $LiNbO_3$-Li cell. The interphase characteristics of the electrodes upon cycling have also been studied by EIS (Figure 4c). It should be noted that the cycled NCM cathode has been replaced here by fresh Li foils. In addition, the electrolyte and separator were also refreshed before the EIS measurements. Two semicircles can be identified in the Nyquist plots, one at high frequencies related to the SEI surface film resistance and another semicircle at low frequencies, which can be attributed to the electrode charge-transfer resistance.[27] For the bare Li anode cell, the fitted values for the SEI resistance significantly increase from 123 (10th cycle) to 405 Ω (100th cycle).

On the other hand, the SEI resistance for the $LiNbO_3$-Li cell increases from 109 (10th cycle) to 234 Ω after 100 cycles. It can be concluded from these results that the SEI formation predominantly occurs at the initial stages of cycling and proceeds at a more moderate rate during prolonged cycling. Furthermore, the impedance comparison shows that the modified-Li anode cell reveals a more moderate SEI resistance increase, thus slowing down the SEI formation during cycling.

The NCM/Li cells were disassembled after cycling for further characterization to investigate the origin of degradation of both Li anodes. Figure 4d shows the surface morphology of the bare Li anode after 10 cycles. Mossy-Li with small particles can initially be observed at the bare Li surface after 10 cycles, and the underlying Li metal displayed a much rougher morphology compared to the pristine Li metal (Figure 1a).

https://doi.org/10.1021/acsaem.1c02278
ACS Appl. Energy Mater. 2021, 4, 10333−10343

The cross section (Figure 4d) also reveals that microstructures are formed at the bare Li anode. After 100 cycles, the SEM top view shows the growth of a highly porous Li surface morphology at the bare Li anode (Figure 4e). The inhomogeneous Li deposition during cycling resulted in highly loose and irregular surface structures.

In the case of the $LiNbO_3$-Li anode (Figure 4f,g), the morphology remains virtually unchanged after 10 cycles compared to its pristine state (Figure 1b), and no mossy-Li is observed at the surface. The corresponding cross-sectional SEM image in Figure 4f also confirms the compact coating of the $LiNbO_3$ layer on the Li metal. A relatively flat surface is found at the $LiNbO_3$-Li anode after 100 cycles, not revealing an open lithium morphology (Figure 4g). The appearing microcracks provide evidence of mechanical stress originating from the anode volume expansion during Li deposition, which negatively influences the $LiNbO_3$-interfacial stability. Moreover, from the cross-sectional SEM image (Figure 4g), it can be concluded that the SEI film at the modified-Li anode is remarkably thin. These results show that the $LiNbO_3$-protected Li anodes facilitate a more uniform and compact Li deposition during cycling with negligible open Li structures. The thin-film protective $LiNbO_3$ coating can effectively limit the growth of the SEI film.

The dissolution of transition-metal ions from the Ni-rich cathode material during cycling is a widely known phenomenon.[28−30] The dissolved metal ions are transported through the separator and transformed into a reduced state at the anode surface. Subsequently, these reduced species also participate in the SEI formation process. They may serve as a catalyst for various side reactions.[31−33] The introduced $LiNbO_3$ protective layer is a poor electronic conductor, inhibiting the metallic-ion reduction at the anode. XPS measurements were therefore carried out to investigate whether the bare Li and $LiNbO_3$-Li anodes might undergo different SEI evolutions during cycling. The results of these XPS measurements, including detailed valence state analyses, are listed in Table 1.

Figure 5 shows the C 1s, O 1s, F 1s, P 2p, and Ni 2p spectra for both anodes after 10 cycles. In the C 1s spectra (Figure 5a), peaks located at 283.9, 287.3, 289.6, and 289.5 eV correspond to C−Li, C−C/C−H, C−O, and C═O (Li_2CO_3), respectively. The C−Li, C−C/C−H, and C−O bonds are attributed to organic components originating from the electrolyte solvent decomposition and polymerization, such as RLi and ROLi.[34] C═O (Li_2CO_3) might result from electrolyte decomposition and the reaction between metallic Li and the gaseous byproduct CO_2 formed in the cell. Both electrodes show similar peaks in the C 1s spectra, except that significantly decreased peak intensities are found for the $LiNbO_3$-protected Li anode. The O 1s spectra are shown in Figure 5b. The peaks are related to Li_2O (527.3 eV), Li_2CO_3, or O═C−O bond originating from $ROCO_2Li$ (528.7 eV). The C−O bond at 531.1 eV originating from RLi is visible at the bare Li surface. The small amount of Li_2O at 527.3 eV can be associated with reactions induced by traces of oxygen and water present in the cell. In contrast, the absence of the Li_2O peak, along with the reduced intensity of the Li_2CO_3 (or O═C−O) and C−O peaks, is found for the $LiNbO_3$-Li anode.

Additionally, peaks at 685.3 eV in the F 1s spectra (Figure 5c) and at 133.1 eV in the P 2p spectra (Figure 5d) can be

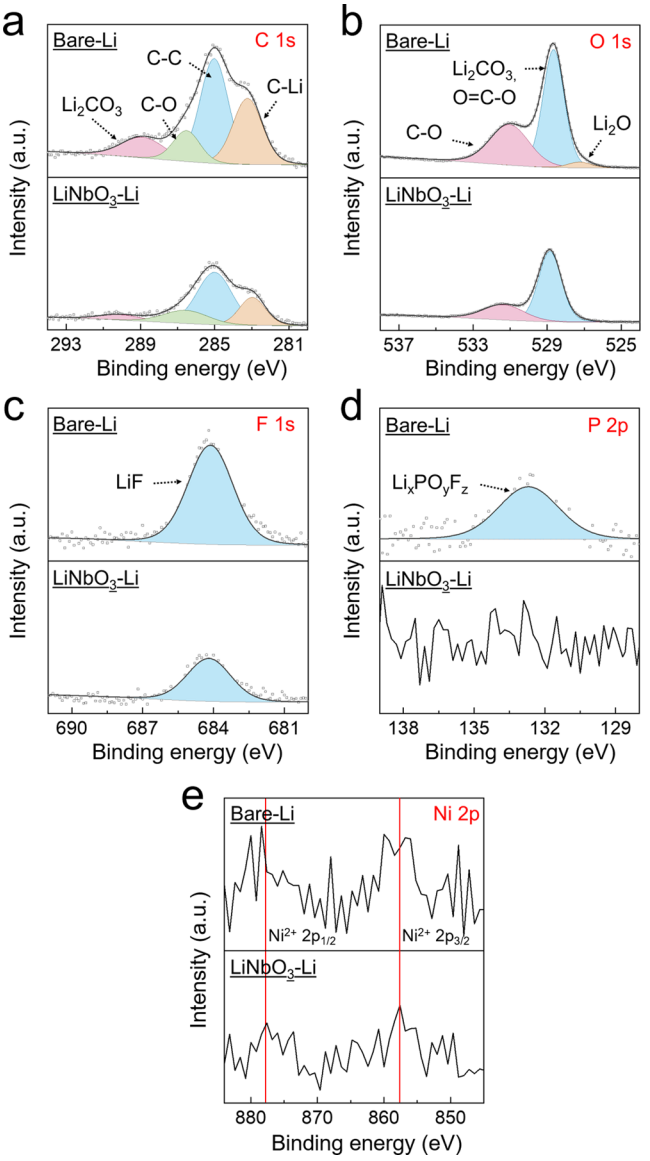

Figure 5. XPS spectra of (a) C 1s, (b) O 1s, (c) F 1s, (d) P 2p, and (e) Ni 2p obtained for both Li anodes after 10 cycles.

Table 1. Summary of XPS Results for Bare Li and $LiNbO_3$-Protected Electrodes

	binding energy (eV)	peak assignment	reference
C 1s	~283.9	C−Li (RLi, lithium alkyl)	24
	~287.3	C−C, C−H	24
	~289.6	C−O (ROLi, lithium alkoxide)	24
	~289.5	C═O	24
	~291.8	C−F	35
O 1s	~527.3	Li_2O	26
	~528.7	Li_2CO_3/O═C−O ($ROCO_2Li$, lithium alkyl carbonates)	26
	~531.1	C−O	26
F 1s	~685.3	LiF	36
	~686.1	Li_xPF_y/$Li_xPO_yF_z$	37
	~687.5	C−F	36
P 2p	~133.1	$Li_xPO_yF_z$	38
	~136.2	Li_xPF_y	38
Ni 2p	~850.1	Ni	33
	~857.8	NiF_2	33

https://doi.org/10.1021/acsaem.1c02278
ACS Appl. Energy Mater. 2021, 4, 10333−10343

assigned to LiF and $Li_xPO_yF_z$, respectively, which results from the decomposition of lithium salt in the electrolyte. Compared to the bare Li anode, a much smaller amount of LiF and no $Li_xPO_yF_z$ is observed at the $LiNbO_3$-Li anode surface after 10 cycles. Furthermore, the signals of the Ni 2p spectra of both anodes only reveal a relatively low resolution (Figure 5e), suggesting that the dissolution and transport of transition-metal ions occurred to some extent during the initial cycles. However, based on the quantitative analyses of the XPS survey scan shown in Figure S2c, the surface of the bare Li anode exhibits a higher atomic ratio of the Ni element after 10 cycles (0.22%) than that of the $LiNbO_3$-Li anode (0.09%). XPS surface analyses of both anodes after 10 cycles show that the reduction rate of metal ions is limited during the initial cycles. Moreover, the initial SEI film predominantly consists of inorganic components, including LiF, Li_2CO_3, Li_2O, and $Li_xPO_yF_z$, accompanied by the generation of a few organic components, such as lithium alkyl (RLi) and lithium alkoxide (ROLi) species.

Furthermore, the surface components of both anodes after long-term cycling have been investigated by XPS. Figure 6 shows the spectra of the corresponding elements after 100 cycles. In the C 1s spectra (Figure 6a), a new peak located at 291.8 eV is found at the bare Li anode, which can be assigned to the C−F bond. A significantly growing C−Li content originating from lithium alkyl is detected at the $LiNbO_3$-Li anode. Accordingly, the O 1s spectra of the bare Li anode after 100 cycles (Figure 6b) are highly consistent with the results obtained after 10 cycles. The peak corresponding to C−O becomes more intense for the $LiNbO_3$-Li anode after prolonged cycling. The F 1s and P 2p spectra indicate the complexity of phosphorous- and fluorine-containing components formed at both long-term cycled anodes. In the F 1s spectra (Figure 6c), two new peaks emerged at the surface of the bare Li anode. The peaks at 686.1 and 687.5 eV correspond to Li_xPF_y (or $Li_xPO_yF_z$) and the C−F bond, respectively, which originated from electrolyte degradation and PVDF migration from the cathode.

Regarding the F 1s spectra of the $LiNbO_3$-Li anode, no C−F species can be found, and the signal of LiF is significantly higher than that of the Li_xPF_y (or $Li_xPO_yF_z$) peaks. Additionally, the P 2p spectra in Figure 6d demonstrate that the phosphorous components at the surfaces are dominated by Li_xPF_y for the bare Li anode and by $Li_xPO_yF_z$ for the $LiNbO_3$-Li anode. It is also worth noting that Ni is identified in both Ni 2p spectra after long-term cycling (Figure 6e): two pairs of peaks can be assigned to metallic Ni at 850.1 eV and NiF_2 at 857.8 eV, which are the reduction states of dissolved Ni ions at the anode surface. Interestingly, according to the semi-quantitative XPS analyses in Figure S2c, the atomic ratio of Ni at the $LiNbO_3$-protected Li anode remained virtually unchanged from 10 cycles (0.09%) to 100 cycles (0.10%). In contrast, the detectable Ni content at the bare Li anode unravels a considerable increase from 0.22% at 10 cycles to 1.05% after 100 cycles. This increase shows that Ni is continuously reduced at the bare Li anode.

From the above XPS analyses, general information about the chemistry of the SEI formation upon anode cycling is provided. For the bare Li anode, apart from the components that have been presented after initial cycling in Figure 5, new species arise upon long-term cycling. These species can be assigned to organic components (lithium alkyl carbonates ($ROCO_2Li$) and PVDF) and inorganic components (Li_xPF_y and NiF_2). PVDF

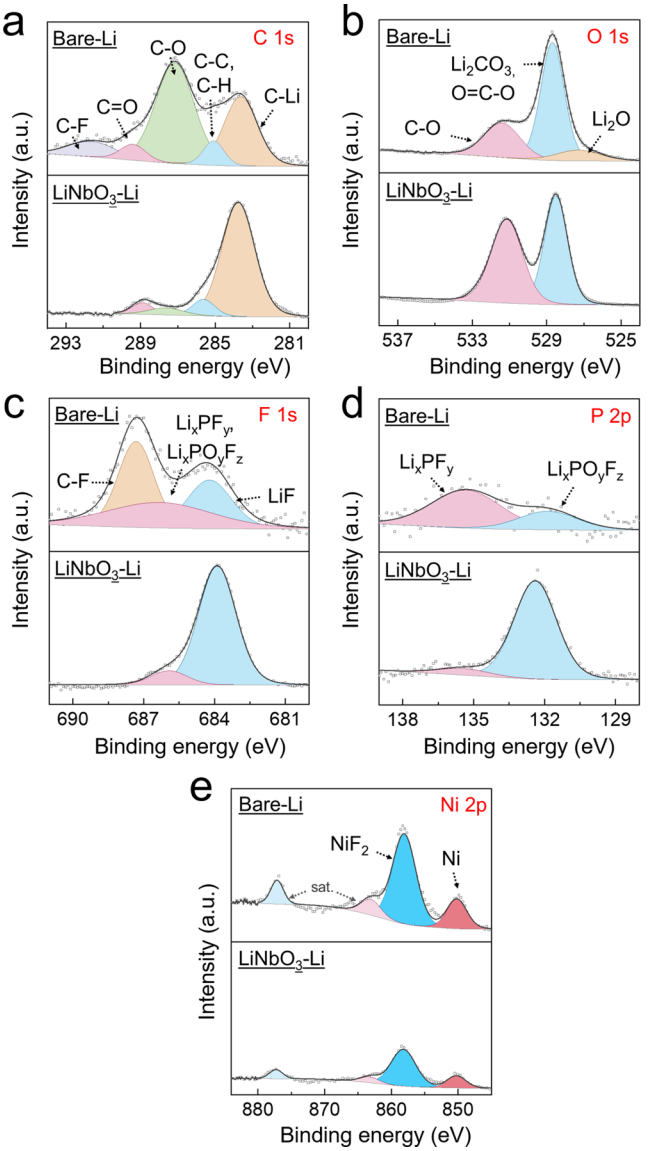

Figure 6. XPS spectra of (a) C 1s, (b) O 1s, (c) F 1s, (d) P 2p, and (e) Ni 2p obtained for the bare Li and $LiNbO_3$-Li anodes after 100 cycles.

can be attributed to the migration of the binder material from the cathode, while NiF_2 is due to the reduction of metal ions crossing the electrolyte.

For the $LiNbO_3$-Li anode, a much more restrained growth of the SEI film can be observed. New components show up after extensive cycling, including $ROCO_2Li$, $Li_xPO_yF_z$, and NiF_2. Also, the absence of PVDF and the barely growing Ni content at the $LiNbO_3$-Li anode demonstrate that the $LiNbO_3$ protective layer appropriately suppressed the chemical crossing from the cathode.

Figure 7a,b schematically shows the development of the SEI layers at the bare Li and protected Li anodes. A loose and fragile SEI film, composed of inorganic rich components, is formed at the bare Li anode at the beginning of cycling, accompanied by uneven lithium deposition and mossy-Li growth. The initially deposited mossy-Li eventually develops into a highly porous structure during cycling due to Li's repeated deposition and stripping. In conclusion, the evolution of the SEI surface layer is a complex process in which many

https://doi.org/10.1021/acsaem.1c02278
ACS Appl. Energy Mater. 2021, 4, 10333−10343

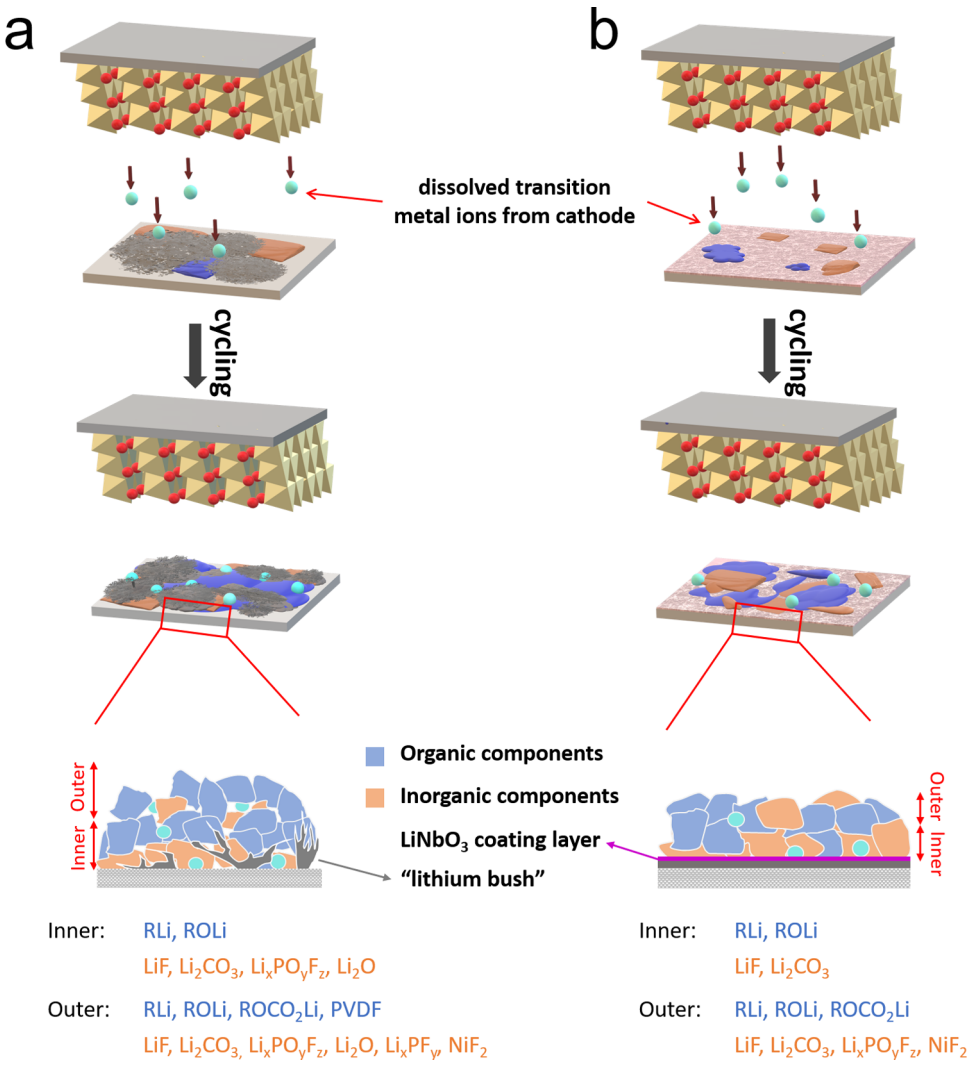

Figure 7. Schematic representation of the SEI film growth at the (a) bare Li and (b) $LiNbO_3$-Li anodes.

components are formed during cycling in both the inner and outer layers.[39] Notably, the presence of PVDF species and the increase of Ni are observed at the bare Li anode surface, indicating the increased impact of the cathode on the performance of the Li anode during cycling.

In contrast, the evolution of the SEI film on the $LiNbO_3$-protected Li anode is a more straightforward process (Figure 7b). First, no porous lithium is formed at the anode surface, implying smooth and uniform lithium deposition and stripping. Second, the lack of PVDF species and the limited amount of Ni formed inside the SEI layer during cycling confirm the stabilizing role of the $LiNbO_3$ protective layer at the Li anode surface. It suppresses the reduction of Ni ions, stemming from the cathode dissolution, at the anode surface.

Although the different evolutions of SEI films on two Li-metal anodes have been discussed above, the detailed underlying mechanisms for SEI growth remain not fully understood. According to previous studies, the catalytic effect of metallic Ni may play a key role in accelerating the SEI growth.[33,40,41] Metallic nanoparticles formed at the anode surface may potentially act as nucleation sites for multiple side reactions due to their high electronic conductivity and surface energy. When a bare Li anode is coupled with a Ni-rich cathode in a complete Li/NMC cell, Ni ions will dissolve into the electrolyte and move through the separator to the anode, where the ions are randomly deposited and embedded into the open SEI film. To make things worse, Li metal itself is already highly reactive toward the electrolyte, as concluded in the storage tests of Figure 2a. Thus, the mossy and open Li structure that emerges upon cycling provides a large specific surface area for these side reactions. Given the additional electronic pathways provided by Ni contamination, exacerbated surface passivation can indeed be expected for bare Li anodes.

On the other hand, in $LiNbO_3$-protected Li anodes, the following aspects explain the observed improvements: (1) $LiNbO_3$ layers efficiently isolate Li metal from direct interaction with the electrolyte, inhibiting side reactions; (2) the growth of Li structures is suppressed by the $LiNbO_3$ layer, while its intrinsically high ionic conductivity guarantees a smooth transfer of Li ions as well as a more uniform Li deposition; (3) the rate of Ni-ion reduction is effectively declined due to the electronically nonconductive $LiNbO_3$ layer, though the dissolution of transition-metal ions accelerates with cycling, and the amount of Ni contamination on the $LiNbO_3$-Li anode is kept relatively stable; and (4) the growth of the SEI film is limited at $LiNbO_3$-protected Li anodes, resulting in a moderate and more compact SEI

https://doi.org/10.1021/acsaem.1c02278
ACS Appl. Energy Mater. 2021, 4, 10333−10343

formation. More detailed investigations from a computational perspective, such as density functional theory calculations, are necessary to understand SEI evolution in more detail.

CONCLUSIONS

Amorphous $LiNbO_3$ thin films deposited by RF sputtering onto Li metal were used as a protective coating on Li-metal anodes. Compared with unprotected bare Li anodes, $LiNbO_3$-protected Li-metal anodes demonstrated an enhanced electrochemical stripping and plating performance in symmetrical cells, with prolonged cycling life and lower polarization. Full cells composed of Ni-rich NCM cathodes and various Li-metal anodes have been assembled to explore the influence of the crossover effect induced by the cathode on the SEI formation process. Electrochemical measurements showed significantly improved cycling stability of NCM/$LiNbO_3$-Li cells with a capacity retention of 80% after 100 cycles, which was considerably higher than that of NCM/bare Li cells.

In addition, postmortem XPS characterization revealed differences in SEI evolution of $LiNbO_3$-protected Li anodes upon cycling. For bare Li anodes, the surface showed a highly loose morphology with various Li structures. In contrast, a more compact and flat structure was observed at the $LiNbO_3$-Li anode surface after cycling, implying uniform Li deposition and more moderate SEI film formation. Furthermore, the chemical composition of the SEI layer during cycling was investigated by XPS. In particular, the migrated PVDF species from the cathode side and reduced Ni states (NiF_2 and Ni) were found in large concentrations at bare Li anodes, indicating that Ni dissolution from the cathode plays a dominant role.

On the other hand, for $LiNbO_3$-protected Li anodes, no PVDF species and a virtually unchanged low amount of Ni content after cycling have been detected. Considering the catalytic role of reduced metal ions, it is expected that $LiNbO_3$ layers prevent the deposition of Ni species inside the SEI layer at metallic Li, thereby favorably influencing the SEI film morphology and, consequently, improving the overall cell performance. Additionally, artificial layers deposited on the cathode, novel electrolyte additives, separator with enhanced selectivity, and protective coatings for Li metal with higher flexibility could further mitigate the reactivity of Li-metal anodes and promote the long-term stability for the next-generation LMBs.

ASSOCIATED CONTENT

Supporting Information

The Supporting Information is available free of charge at https://pubs.acs.org/doi/10.1021/acsaem.1c02278.

Additional figures including XRD and additional XPS data (PDF)

AUTHOR INFORMATION

Corresponding Author

Peter H. L. Notten − *Eindhoven University of Technology, 5600 MB Eindhoven, The Netherlands; IEK-9, Forschungszentrum Jülich, D-52425 Jülich, Germany; University of Technology Sydney, Sydney, NSW 2007, Australia;* orcid.org/0000-0003-4907-8426; Email: p.h.l.notten@tue.nl

Authors

Ming Jiang − *Eindhoven University of Technology, 5600 MB Eindhoven, The Netherlands; IEK-9, Forschungszentrum Jülich, D-52425 Jülich, Germany*

Qian Zhang − *IEK-9, Forschungszentrum Jülich, D-52425 Jülich, Germany; RWTH Aachen University, D-52074 Aachen, Germany*

Dmitri L. Danilov − *Eindhoven University of Technology, 5600 MB Eindhoven, The Netherlands; IEK-9, Forschungszentrum Jülich, D-52425 Jülich, Germany*

Rüdiger-A. Eichel − *IEK-9, Forschungszentrum Jülich, D-52425 Jülich, Germany; RWTH Aachen University, D-52074 Aachen, Germany;* orcid.org/0000-0002-0013-6325

Complete contact information is available at: https://pubs.acs.org/10.1021/acsaem.1c02278

Notes

The authors declare no competing financial interest.

ACKNOWLEDGMENTS

M.J. gratefully acknowledges a fellowship support by the China Scholarship Council.

REFERENCES

(1) Manthiram, A. A reflection on lithium-ion battery cathode chemistry. *Nat. Commun.* **2020**, *11*, No. 1550.

(2) Zhu, G. L.; Zhao, C. Z.; Huang, J. Q.; He, C.; Zhang, J.; Chen, S.; Xu, L.; Yuan, H.; Zhang, Q. Fast Charging Lithium Batteries: Recent Progress and Future Prospects. *Small* **2019**, *15*, No. 1805389.

(3) Wen, L.; Liang, J.; Chen, J.; Chu, Z. Y.; Cheng, H. M.; Li, F. Smart Materials and Design toward Safe and Durable Lithium Ion Batteries. *Small Methods* **2019**, *3*, No. 1900323.

(4) Fan, X.; Chen, L.; Borodin, O.; Ji, X.; Chen, J.; Hou, S.; Deng, T.; Zheng, J.; Yang, C.; Liou, S. C.; Amine, K.; Xu, K.; Wang, C. Non-flammable electrolyte enables Li-metal batteries with aggressive cathode chemistries. *Nat. Nanotechnol.* **2018**, *13*, 715−722.

(5) Xu, W.; Wang, J.; Ding, F.; Chen, X.; Nasybulin, E.; Zhang, Y.; Zhang, J.-G. Lithium metal anodes for rechargeable batteries. *Energy Environ. Sci.* **2014**, *7*, 513−537.

(6) Park, S. J.; Hwang, J. Y.; Yoon, C. S.; Jung, H. G.; Sun, Y. K. Stabilization of Lithium-Metal Batteries Based on the in Situ Formation of a Stable Solid Electrolyte Interphase Layer. *ACS Appl. Mater. Interfaces* **2018**, *10*, 17985−17993.

(7) Choi, J. W.; Aurbach, D. Promise and reality of post-lithium-ion batteries with high energy densities. *Nat. Rev. Mater.* **2016**, *1*, No. 16013.

(8) Li, N. W.; Yin, Y. X.; Yang, C. P.; Guo, Y. G. An Artificial Solid Electrolyte Interphase Layer for Stable Lithium Metal Anodes. *Adv. Mater.* **2016**, *28*, 1853−1858.

(9) Wang, L.; Wang, Q.; Jia, W.; Chen, S.; Gao, P.; Li, J. Li metal coated with amorphous Li_3PO_4 via magnetron sputtering for stable and long-cycle life lithium metal batteries. *J. Power Sources* **2017**, *342*, 175−182.

(10) Xu, R.; Zhang, X. Q.; Cheng, X. B.; Peng, H. J.; Zhao, C. Z.; Yan, C.; Huang, J. Q. Artificial Soft-Rigid Protective Layer for Dendrite-Free Lithium Metal Anode. *Adv. Funct. Mater.* **2018**, *28*, No. 1705838.

(11) Cheng, X. B.; Zhang, R.; Zhao, C. Z.; Zhang, Q. Toward Safe Lithium Metal Anode in Rechargeable Batteries: A Review. *Chem. Rev.* **2017**, *117*, 10403−10473.

(12) Wang, D.; Zhang, W.; Zheng, W.; Cui, X.; Rojo, T.; Zhang, Q. Towards High-Safe Lithium Metal Anodes: Suppressing Lithium Dendrites via Tuning Surface Energy. *Adv. Sci.* **2017**, *4*, No. 1600168.

(13) Cheng, X. B.; Zhang, R.; Zhao, C. Z.; Wei, F.; Zhang, J. G.; Zhang, Q. A Review of Solid Electrolyte Interphases on Lithium Metal Anode. *Adv. Sci.* **2016**, *3*, No. 1500213.
(14) Sun, Y.; Zhao, Y.; Wang, J.; Liang, J.; Wang, C.; Sun, Q.; Lin, X.; Adair, K. R.; Luo, J.; Wang, D.; Li, R.; Cai, M.; Sham, T. K.; Sun, X. A Novel Organic "Polyurea" Thin Film for Ultralong-Life Lithium-Metal Anodes via Molecular-Layer Deposition. *Adv. Mater.* **2019**, *31*, No. 1806541.
(15) Cha, E.; Patel, M. D.; Park, J.; Hwang, J.; Prasad, V.; Cho, K.; Choi, W. 2D MoS_2 as an efficient protective layer for lithium metal anodes in high-performance Li-S batteries. *Nat. Nanotechnol.* **2018**, *13*, 337−344.
(16) Liu, Y.; Lin, D.; Yuen, P. Y.; Liu, K.; Xie, J.; Dauskardt, R. H.; Cui, Y. An Artificial Solid Electrolyte Interphase with High Li-Ion Conductivity, Mechanical Strength, and Flexibility for Stable Lithium Metal Anodes. *Adv. Mater.* **2017**, *29*, No. 1605531.
(17) Ye, H.; Zheng, Z. J.; Yao, H. R.; Liu, S. C.; Zuo, T. T.; Wu, X. W.; Yin, Y. X.; Li, N. W.; Gu, J. J.; Cao, F. F.; Guo, Y. G. Guiding Uniform Li Plating/Stripping through Lithium-Aluminum Alloying Medium for Long-Life Li Metal Batteries. *Angew. Chem., Int. Ed.* **2019**, *58*, 1094−1099.
(18) Huang, Z.; Zhou, G.; Lv, W.; Deng, Y.; Zhang, Y.; Zhang, C.; Kang, F.; Yang, Q.-H. Seeding lithium seeds towards uniform lithium deposition for stable lithium metal anodes. *Nano Energy* **2019**, *61*, 47−53.
(19) Liu, K.; Pei, A.; Lee, H. R.; Kong, B.; Liu, N.; Lin, D.; Liu, Y.; Liu, C.; Hsu, P. C.; Bao, Z.; Cui, Y. Lithium Metal Anodes with an Adaptive "Solid-Liquid" Interfacial Protective Layer. *J. Am. Chem. Soc.* **2017**, *139*, 4815−4820.
(20) Kazyak, E.; Wood, K. N.; Dasgupta, N. P. Improved Cycle Life and Stability of Lithium Metal Anodes through Ultrathin Atomic Layer Deposition Surface Treatments. *Chem. Mater.* **2015**, *27*, 6457−6462.
(21) Fang, S.; Jackson, D.; Dreibelbis, M. L.; Kuech, T. F.; Hamers, R. J. Anode-originated SEI migration contributes to formation of cathode-electrolyte interphase layer. *J. Power Sources* **2018**, *373*, 184−192.
(22) Mao, C.; Ruther, R. E.; Geng, L.; Li, Z.; Leonard, D. N.; Meyer, H. M., 3rd; Sacci, R. L.; Wood, D. L., 3rd Evaluation of Gas Formation and Consumption Driven by Crossover Effect in High-Voltage Lithium-Ion Batteries with Ni-Rich NMC Cathodes. *ACS Appl. Mater. Interfaces* **2019**, *11*, 43235−43243.
(23) Zhang, J.-N.; Li, Q.; Wang, Y.; Zheng, J.; Yu, X.; Li, H. Dynamic evolution of cathode electrolyte interphase (CEI) on high voltage $LiCoO_2$ cathode and its interaction with Li anode. *Energy Storage Mater.* **2018**, *14*, 1−7.
(24) Lee, H.; Lim, H.-S.; Ren, X.; Yu, L.; Engelhard, M. H.; Han, K. S.; Lee, J.; Kim, H.-T.; Xiao, J.; Liu, J.; Xu, W.; Zhang, J.-G. Detrimental Effects of Chemical Crossover from the Lithium Anode to Cathode in Rechargeable Lithium Metal Batteries. *ACS Energy Lett.* **2018**, *3*, 2921−2930.
(25) Betz, J.; Brinkmann, J. P.; Nölle, R.; Lürenbaum, C.; Kolek, M.; Stan, M. C.; Winter, M.; Placke, T. Cross Talk between Transition Metal Cathode and Li Metal Anode: Unraveling Its Influence on the Deposition/Dissolution Behavior and Morphology of Lithium. *Adv. Energy Mater.* **2019**, *9*, No. 1900574.
(26) Langdon, J.; Manthiram, A. Crossover Effects in Batteries with High-Nickel Cathodes and Lithium-Metal Anodes. *Adv. Funct. Mater.* **2021**, *31*, No. 2010267.
(27) An, S. J.; Li, J.; Daniel, C.; Meyer, H. M., 3rd; Trask, S. E.; Polzin, B. J.; Wood, D. L., 3rd Electrolyte Volume Effects on Electrochemical Performance and Solid Electrolyte Interphase in Si-Graphite/NMC Lithium-Ion Pouch Cells. *ACS Appl. Mater. Interfaces* **2017**, *9*, 18799−18808.
(28) Ko, D.-S.; Park, J.-H.; Park, S.; Ham, Y. N.; Ahn, S. J.; Park, J.-H.; Han, H. N.; Lee, E.; Jeon, W. S.; Jung, C. Microstructural visualization of compositional changes induced by transition metal dissolution in Ni-rich layered cathode materials by high-resolution particle analysis. *Nano Energy* **2019**, *56*, 434−442.
(29) Kim, T.; Ono, L. K.; Fleck, N.; Raga, S. R.; Qi, Y. Transition metal speciation as a degradation mechanism with the formation of a solid-electrolyte interphase (SEI) in Ni-rich transition metal oxide cathodes. *J. Mater. Chem. A* **2018**, *6*, 14449−14463.
(30) Zhang, S. S. Problems and their origins of Ni-rich layered oxide cathode materials. *Energy Storage Mater.* **2020**, *24*, 247−254.
(31) Li, W. Review—An Unpredictable Hazard in Lithium-ion Batteries from Transition Metal Ions: Dissolution from Cathodes, Deposition on Anodes and Elimination Strategies. *J. Electrochem. Soc.* **2020**, *167*, No. 090514.
(32) Jung, R.; Linsenmann, F.; Thomas, R.; Wandt, J.; Solchenbach, S.; Maglia, F.; Stinner, C.; Tromp, M.; Gasteiger, H. A. Nickel, Manganese, and Cobalt Dissolution from Ni-Rich NMC and Their Effects on NMC622-Graphite Cells. *J. Electrochem. Soc.* **2019**, *166*, A378−A389.
(33) Kim, J.; Ma, H.; Cha, H.; Lee, H.; Sung, J.; Seo, M.; Oh, P.; Park, M.; Cho, J. A highly stabilized nickel-rich cathode material by nanoscale epitaxy control for high-energy lithium-ion batteries. *Energy Environ. Sci.* **2018**, *11*, 1449−1459.
(34) Wang, Q.; Jiang, L.; Yu, Y.; Sun, J. Progress of enhancing the safety of lithium ion battery from the electrolyte aspect. *Nano Energy* **2019**, *55*, 93−114.
(35) Liu, W.; Li, J.; Li, W.; Xu, H.; Zhang, C.; Qiu, X. Inhibition of transition metals dissolution in cobalt-free cathode with ultrathin robust interphase in concentrated electrolyte. *Nat. Commun.* **2020**, *11*, No. 3629.
(36) Niehoff, P.; Winter, M. Composition and growth behavior of the surface and electrolyte decomposition layer of/on a commercial lithium ion battery $Li_xNi_{1/3}Mn_{1/3}Co_{1/3}O_2$ cathode determined by sputter depth profile X-ray photoelectron spectroscopy. *Langmuir* **2013**, *29*, 15813−15821.
(37) Li, W.; Lucht, B. L. Lithium-Ion Batteries: Thermal Reactions of Electrolyte with the Surface of Metal Oxide Cathode Particles. *J. Electrochem. Soc.* **2006**, *153*, A1617.
(38) Li, Q.; Wang, Y.; Wang, X.; Sun, X.; Zhang, J. N.; Yu, X.; Li, H. Investigations on the Fundamental Process of Cathode Electrolyte Interphase Formation and Evolution of High-Voltage Cathodes. *ACS Appl. Mater. Interfaces* **2020**, *12*, 2319−2326.
(39) Li, D.; Danilov, D.; Zhang, Z.; Chen, H.; Yang, Y.; Notten, P. H. L. Modeling the SEI-Formation on Graphite Electrodes in $LiFePO_4$ Batteries. *J. Electrochem. Soc.* **2015**, *162*, A858−A869.
(40) Li, W.; Kim, U. H.; Dolocan, A.; Sun, Y. K.; Manthiram, A. Formation and Inhibition of Metallic Lithium Microstructures in Lithium Batteries Driven by Chemical Crossover. *ACS Nano* **2017**, *11*, 5853−5863.
(41) Li, W.; Dolocan, A.; Oh, P.; Celio, H.; Park, S.; Cho, J.; Manthiram, A. Dynamic behaviour of interphases and its implication on high-energy-density cathode materials in lithium-ion batteries. *Nat. Commun.* **2017**, *8*, No. 14589.

https://doi.org/10.1021/acsaem.1c02278
ACS Appl. Energy Mater. 2021, 4, 10333−10343